

СООБЩЕНИЯ
ОБЪЕДИНЕННОГО
ИНСТИТУТА
ЯДЕРНЫХ
ИССЛЕДОВАНИЙ

Дубна

96-411

E13-96-411

L.M.Soroko

MESO-OPTICS FOR SCIENCE AND INDUSTRY

1996

1. INTRODUCTION

The term "MESO-OPTICS" was originated in 1982 [1] and has been accepted officially in 1984 [2] on ICO-13 Congress, Sapporo, Japan (ICO-International Commission on Optics).

Meso-optics is a part of optics in which the properties of the conical wave fields are studied. The main feature of meso-optics is that by means of the meso-optical elements we can perform nontrivial transformations of space coordinates at which the straight line object is transformed as a whole into two point like images having diffraction limited dimensions. Therefore conical wave fields can be considered as peculiar eigen-functions of the meso-optical operator defined over straight line objects. Due to this the information about the position of the straight line object in 3D space is defined exhaustedly by two conical waves, each at different camera angle.

In the traditional optics the imaging objective performs transformation of the point-like object into the point-like image, and the position of the point-like object in 3D space is defined by two spherical waves at two camera angles. Here the spherical wave can be considered as a peculiar eigen-function of the optical operator being defined over point-like objects. To observe straight line segment by means of the traditional objective we must subdivide each such object into a corresponding set of point like elements and transport in space this information via set of the spherical waves.

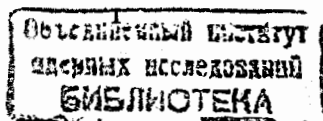
Dualism between point-like objects and spherical waves in traditional optics is complimented in meso-optics by dualism between straight line segments and conical waves. The meso-optical operator transforms each conical wave into a delta function of space coordinates.

The information compression in the case of objects such as straight line objects arises in meso-optics quite naturally, occurs in the real time and does not require computer processing of the initial 3D information. Each meso-optical element does not subdivide the straight line object into a set of the point like elements and accepts it as a whole. There are no scanning operations along straight line objects as well as scanning operation in depth. Due to such on-line information compression, meso-optical devices offer high productivity in the selective observation of the straight line particle tracks in nuclear emulsion technique.

Theoretical and experimental investigations performed in the Laboratory of Nuclear Problems of the Joint Institute for Nuclear Research [3] demonstrated that meso-optical element with ring response accomplishes the on-line transformation of the straight line particle track image into two point-like spots.

This paper represents a concise overview of the meso-optical devices which have high productivity. For example, the rapidity of all these meso-optical devices is 100-300 times higher than the rapidity offered by devices constructed on the basis of the traditional optics.

The first such device is meso-optical Fourier transform microscope for nuclear emulsion which does not require the depth scanning. This device sees only straight line particle tracks and determines instantly the position of the particle track in space



including two angular coordinates. The unique prototype of the meso-optical Fourier transform microscope has been made in JINR [3,4].

The next device is the confocal meso-optical microscope for selective observation of the vertical particle tracks which is now in progress.

The conical wave fields produces the longitudinal interference of light which has been observed first in LNP JINR [5,6,7]. On the basis of this phenomenon we can construct meso-optical profilometer and meso-optical keratometer, described in this concise overview.

Meso-optical undulator installed into the electron beam of the photon source accomplishes the transformation of the synchrotron radiation conical wave fields into the spherical waves and then into the point-like spot. The self-focusing undulator described next, transforms directly the synchrotron radiation into the narrow ring and does not require any focusing units. Both these devices resolve the problem of high density heat flow in the point-like diaphragm used for transportation of the synchrotron radiation.

Meso-optical interferometer and meso-optical autocollimator perform in the real time the precise control of the conical surfaces both internal and external.

It is interesting to note that just meso-optics gave rise naturally to principally new stereoscopic optical microscope which gives high depth selectivity and large field of view.

2. MESO-OPTICAL FOURIER TRANSFORM MICROSCOPE

Schematic diagram of the Stereoscopic meso-optical Fourier transform microscope with double focusing is shown in Fig. 1 [8]. There are two stereoscopic arms, each at the angle $\pm 30^\circ$ with respect to the main axis of symmetry. The nuclear emulsion layer is illuminated by the astigmatic convergent light beam with sagittal crossover inside the nuclear emulsion layer and with meridional crossover in the plane where the photosensitive matrix of the CCD-TV-camera is located.

Two cylindrical objectives 2 operate as two independent 1D projection systems. The diffracted light rays gathered by the cylindrical objective 2 are focused in the meridional cross section into the bright spot on the photosensitive matrix 6 of the CCD-TV-camera. To transport two meso-optical images onto CCD-matrix, an optical interface with two pairs of plane mirrors 3,5 and with one double mirror 4 is used. The geometrical dimensions of each meso-optical image, $\delta\rho$ and $\delta\omega$, define the resolution of this microscope along transversal coordinate X and along angular coordinate $\theta_{X,Y}$. The linear magnification of the whole optical interface is equal to $M = 4 : 1$.

The construction of the meso-optical block with one frontal spherical lens 1 and with two cylindrical objectives 2, mounted rigidly on the organic glass support is shown in Fig. 2 [8].

One typical small angle scattering event of the particle with scattering angle $\theta_{X,Y}$, shown in Fig. 3 at three different longitudinal coordinates X , is transformed by this stereoscopic microscope with double focusing into three different meso-optical pictures (Fig. 4). In the picture, observed at the longitudinal coordinate $X = 4.413$ mm, we

see one pair of meso-optical images, L and R , of the particle track A . In the picture, emerged at the longitudinal coordinate $X = 4.593$ mm, we see two pairs of meso-optical images, one pair from the particle track A , and another pair from the particle track B . In the position of the event with longitudinal coordinate $X = 4.842$ mm we see only one pair of meso-optical images, from the particle track B .

The experimental data which have been gathered over the length of the particle track 6 mm enables one to check the genetic unity of the particle tracks going from the vertex point, to fix the small angle scattering events and to isolate some local geometrical distortions of the nuclear emulsion layer [9].

For example, the effect of the global forced bending of the nuclear emulsion glass support was detected and was estimated as $d\theta_z/dY = 2'$ (angular minute) per mm.

Meso-optical Fourier transform microscope shows exotic properties: large depth of focus [3], ring stereo-effect [3], depth viewing without depth scanning [12], meso-optical counterpart of the classical Moiré-effect [10] as well as new technique of the particle track curvature measurement [11]. Some variants of the meso-optical Fourier transform microscope are described in the papers [13,14,15].

3. CONFOCAL MESO-OPTICAL MICROSCOPES FOR SELECTIVE OBSERVATION OF THE VERTICAL PARTICLE TRACKS

Complete scheme of the confocal microscope for selective observation of the vertical particle tracks with convergent and divergent geometries of the light rays is shown in Fig. 5 [16]. The laser 1 produces a collimated monochromatic light beam, which is reflected from the plane mirror 2 and is directed into the cylindrical interference illuminating system 3. The latter is provided with two eccentric cylindrical lenses. The illuminating interference pattern is located in the nuclear emulsion layer 5 of the depth h . The diffracted light is picked up by the imaging objective 6 with focal length which is 1.62 times of the focal length of the illuminating objective 3. The objective 8 and the pinhole 9 direct the diffracted light onto the point-like photosensitive element 10.

The scanning operations in this microscope are performed without Z -scanning in depth. The $(X - Y)$ stage of this microscope accomplishes $(X - Y)$ scanning operations prescribed by the program stored in the computer 11. In the case of six vertical particle tracks over the square to be scanned (Fig. 6), the first scanning operation is performed along X -axis by means of the illuminating region in the form of narrow "fens" as in the wide-row drilling. After the first scanning operation we receive 1D function $f(X)$, having six picks. The coordinates of these picks, X_1, \dots, X_6 , of the function $f(X)$ define the positions of the $(X - Y)$ stage of the microscope, at which the vertical particle tracks 1, ..., 6 are falling successively at the centers of the illuminating region.

Before the second scanning operation, the imaging interference system 7 is to be rotated through the angle 90° in its plane. In this configuration the response of the microscope has a point-like structure, as two line responses of systems 3 and 7 are now mutually perpendicular. The second scanning operations are performed six-fold

along Y -axis at X -coordinates X_1, \dots, X_6 , which were stored in the computer 11 after the first scanning operations. Now we have six functions $f_1(Y), \dots, f_6(Y)$ versus Y -coordinate. The positions of six vertical particle tracks to be searched for are defined by six pairs of coordinates $(X_1, Y_1), \dots, (X_6, Y_6)$, where Y_1, \dots, Y_6 are the position coordinates of the maxima of six functions $f_1(Y), \dots, f_6(Y)$.

In general case of N vertical particle tracks over the region to be scanned we must accomplish one 1D scanning with N picks in the function $f(X)$ and then N 1D scannings with one pick in each 1D plot. Thus the total number of 1D scanning is equal to $(N+1)$. In the case of the quadrate region with sides 5 mm length, we must perform $5 \cdot 10^3 (N+1)$ digital measurements with spatial resolution of the order of $1 \mu\text{m}$. Meanwhile in the traditional microscope the number of digital measurements is equal to $(5 \cdot 10^3)^2 \cdot 30$, with number of the measurements along Z -axis in depth being equal to 30. The factor of merits is equal to $k = \frac{(5 \cdot 10^3)^2 \cdot 30}{5 \cdot 10^3 (N+1)} = \frac{15 \cdot 10^4}{(N+1)}$. For $N = 25$, the number of the particle tracks, to be searched for, we have $k = 5.8 \cdot 10^3 : 1$.

In [17] there is described meso-optical confocal microscope based on the caustic phenomenon. The scheme of this microscope is shown in Fig. 7. The illuminating cylindrical half-lens L_1 produces the caustic interference pattern shown in Fig. 8. The nuclear emulsion layer is placed in the vicinity of the focus of the half-lens L_1 and is oriented perpendicular to the external light rays of the caustic pattern. The optical stop S absorbs all internal light rays. The imaging cylindrical half-lens L_2 focuses the light rays of the external part of the caustic interference fringes. The width of the region, where two systems of the interference fringes, one from the illuminating half lens L_1 and another from the imaging half-lens L_2 , are overlapped, can be controlled by transversal moving of these two half-lenses. A typical example of such overlapping is shown in Fig. 7 for the case of the total response width equal to $\Delta/3$.

4. LONGITUDINAL INTERFERENCE OF THE CONICAL WAVES

The longitudinal interference of the diffraction free wave fields as a new phenomenon in meso-optics and experimental arrangements proposed for observation of such phenomenon were described in [5,6,7]. To observe this phenomenon we use two coaxial conical waves defined by two wave vectors \vec{k}_1 and \vec{k}_2 of the same wave length: $|\vec{k}_1| = |\vec{k}_2|$ (Fig. 9). In the meridional cross section of these coaxial wave fronts in the region of their mutual superpositions we see interference fringes oriented along the bisectrix of the angle between two wave vectors \vec{k}_1 and \vec{k}_2 . The period of these fringes is equal to $a = \lambda / \sin(\theta_2 - \theta_1)$, where θ_2 and θ_1 are the angles between wave vectors \vec{k}_1 and \vec{k}_2 with optical axis of the system, respectively. The orientation angle θ_0 of these interference fringes with respect to the optical axis of the system is equal to $\theta_0 = \frac{1}{2}(\theta_1 + \theta_2)$. Each point of this meridional cross section corresponds to a circle. Only points on the optical axis are fixed. The period A of this on-axis light intensity modulation shown in the bottom of Fig. 11 is equal to $A = \lambda / \sin(\theta_2 - \theta_1) \cdot \sin \frac{\theta_2 + \theta_1}{2}$.

Among many possible experimental setups suggested for observation of the longitudinal interference of the light [5] we chose a technique with two narrow coaxial

transmitting rings as the most accessible one. This experimental arrangement is shown in Fig. 10. The collimated beam of light from laser 1 is transformed by the objective lens 2 into the convergent beam of light with focus in the pinhole of the screen 3. The second objective lens 4 produces the single mode beam of light which illuminates the screen 5 with narrow coaxial transmitting rings. The screen 6 restricts the number of the narrow coaxial transmitting rings which contribute to the observed interference picture.

The system of 10 narrow coaxial transmitting rings with spacing $200 \mu\text{m}$ was fabricated by the technique described in [18].

The components of the diffracted light from each transmitting ring are propagated initially separately, then they are mutually overlapped in the vicinity of the optical axis of the system. The objective 7 produces the image of the interference picture in one of the plane perpendicular to the optical axis of the system on the photofilm 8. Different parts of the space of the length l_3 with various evolution stages of the longitudinal interference are shown in Fig. 11. Each plane of this volume is observed by means of the objective 7. In the plane A we see directly the narrow transmitting rings in focus of this objective. In the plane B some kind of self-imaging of the Talbot type can be observed; in the plane C , only partial overlapping of the adjacent coaxial light components. In the region D we see complete overlapping of these components at some distances from the optical axis. Only in the region E the interference picture approaches the optical axis of the system from all azimuthal directions.

The photo of two coaxial transmitting rings in the plane A is shown in Fig. 12. The interference picture in the plane C is presented in Fig. 13, and the picture in the region D is given in Fig. 14. The interference fringes in the region E are shown in Fig. 15.

The position of maxima and minima of the longitudinal modulation of the light intensity on the optical axis is given in Fig. 16. As the angle between two wave vectors \vec{k}_1 and \vec{k}_2 is very small, $\sim 10^{-4}$ radian, the period A of this modulation is of the order of 10 mm. There were estimated 12 maxima and minima on the optical axis of the system. The period A is a slowly varying function of Z -coordinate. This is a natural consequence of the fact that each narrow transmitting ring contributes to the interference pattern as a point-like light source and due to this the angle between wave vectors \vec{k}_1 and \vec{k}_2 is varying inversely proportional to the distance from the screen 5 to the observation point.

The longitudinal interference of the conical waves described above can be used to pick up, fast and remotely, the profile of the external surface of the object. Here we describe confocal meso-optical keratometer [7]. The principle construction of the confocal meso-optical keratometer with central light beam is shown in Fig. 17. This device is provided with point light source 1, optical collimator 2, plane mirror 3, internal and external conical mirrors 4 and 5 of the illuminating unit, conical mirror of the observing unit 6, point-like photodetector 7, moving stage with position encoder 8 and computer memory block 9. The internal mirror 4 has a hole for central light beam. The longitudinal interference is produced by central plane beam and by conical wavefront propagating from external conical mirror 5. The point photode-

ector 7 sees the points in the vicinity of the optical axis over the length range L . To get high noise immunity, the internal diameter D_2 of the observing conical mirror 6 and the external diameter D_1 of the conical mirror 5 are chosen according to the equation $D_1/D_2 = d_1/d_2 \cong 1.62$; $d_1 = D_2$. In this design of the confocal meso-optical keratometer the first side-lobe of the point spread function of the conical mirror 5 does coincide with the first zero of the point spread function of the conical mirror of the observing unit 6. Therefore the overall point spread function of this device does not have practically side-lobes with intensity of the order of 10^{-3} from the central maximum. The lens equivalent of this device having three coaxial axicons instead of the device with three conical mirrors can be offered as well.

5. MESO-OPTICAL UNDULATOR

Relativistic electrons moving in the magnetic field produce synchrotron radiation directed along velocity vectors of electrons \vec{v} inside the angular aperture of the order of $\theta_{SR} \sim 1/\gamma$, where γ — relativistic factor of electrons, $E = \gamma m_0 c^2$ — its energy, and m_0 — its rest mass.

To increase the intensity of synchrotron radiation, an undulator with transversal periodic magnetic field is used nowadays.

The finite length L of the undulator provides some problems in transportation and focusing of the undulator radiation. For observation optical system with small depth of focus we see sharply only small part of the undulator. To focus the side ways going undulator radiation we use inverse meso-optical element shown in Fig. 18 [19]. The first meso-optical element 2 transforms the conical wavefront of radiation with wavelength λ_1 into a ring-shaped focus. The focused radiation is transmitted through the screen with narrow ring-shaped slit 3, which accomplishes premonochromatization of the radiation, by rejecting any other wave lengths with $\lambda \neq \lambda_1$. The coherent radiation, gathered from the full length of the undulator, is focused into the point on the optical axis by means of the second inverse meso-optical element 4. The angular aperture of the first inverse meso-optical objective 2 is much greater than the effective angular aperture of the conventional lens and the diameter of the ring-shaped slit is much greater than the diameter of the pinhole used in the conventional undulators. Another advantage of the meso-optical undulator shown in Fig. 18 is that radiation before the diaphragm 5 is partially monochromatized. Radiation issued from the sources, evenly distributed over the undulator length L , is focused into the point-like spot without any focusing problems inherent to the conventional optics. Besides, some technical cooling problems of the ring-shaped slit 3 are facilitated because of the larger length of the heat exchanger region.

The most remarkable feature of the undulator radiation is the dependence of the wavelength λ from the observation angle θ , defined by the equation

$$\lambda(\theta) = \frac{d_0}{2\gamma^2}(1 + \gamma^2\theta^2 + K), \quad (1)$$

d_0 is the period of the transversal magnetic field of the undulator, and the magnetic

deflection parameter K is equal to $K = 0.934 B_0 d_0$, where peak magnetic field B_0 is expressed in Tesla, and d_0 in cm. For undulator $K < 4$, and for wigglers $K > 10$.

Therefore the wavelength observed at angle θ , can be controlled by the undulator period d_0 .

Figure 19 shows a self-focusing undulator [19], in which the period length d_0 of the transversal magnetic field is a slowly decreasing function of Z -coordinate. The periods of the undulator blocks at the input, d_{in} , and that at the output, d_{out} , of the undulator must be chosen according to the equations

$$\left. \begin{aligned} d_{in} &= 2\gamma^2\lambda/(1 + \gamma^2\theta_1^2 + K), \\ d_{out} &= 2\gamma^2\lambda/(1 + \gamma^2\theta_2^2 + K), \end{aligned} \right\} \quad (2)$$

where

$$\left. \begin{aligned} \gamma\theta_1 &= 1 - L/2f, \\ \gamma\theta_2 &= 1 + L/2f, \end{aligned} \right\} \quad (3)$$

and f is the distance from the center of the self-focusing undulator to the plane where a ring-shaped focus is observed. The undulator period is the decreasing linear function of Z coordinate.

As was shown in Fig. 3 of Ref. [10], the base of the first harmonic peak for $K = 0.515$ exhibits small interference ripples near the main peak which are induced by the sharp truncation of the periodic structure of the undulator magnet along Z -axis. Sometimes the spectral response of this undulator can hinder the running of experiments with high spectral precision, because of the small dynamic range of the whole device. To overcome this disadvantage of the conventional undulator, these sidelobes in the spectral response of the undulator must be suppressed. For this we must withdraw the sharp truncation of the periodic structure of the undulator magnetic field. This can be achieved by varying the thickness t of the undulator magnetic element, made of soft magnetic material. The needed variation of the thickness $t(Z)$ is given by the equation

$$t(Z) = t_0 \exp[-A(Z - Z_0)^2/L^2], \quad (4)$$

where X_0 is the coordinate of the undulator center, and A is a constant, chosen in the range $2.2 \leq A \leq 2.4$. This apodized undulator is shown in Fig. 20 as a model with five periods. The amplitude of the electron trajectory and the intensity of the undulator radiation are changing smoothly along undulator axis, being minimal at the extreme points and maximal in the center of the undulator. As the amplitude of the electron trajectory is varying as truncated Gaussian, Eq. (4), the structure of the observed spectral line will be close to Gaussian with very weak side lobes. This feature of the suggested undulator offers high dynamical spectral range and permits to accomplish the precise measurements in the spectral region very close to the central absorption line.

6. MESO-OPTICAL CONICOMETERS

To solve the problem of the fast precise control of the industrial parts with external conical surfaces, an autocollimator device with three conical mirrors was suggested [21] (Fig. 21). The collimated light beam from the source 1 transverses two beam-splitters, 2 and 3, experiences reflections from the central conical mirror and from two ring-shaped conical mirrors. The external conical surface of the industrial part 6 is illuminated in autocollimator mode from all azimuthal directions simultaneously, if the conical angle of the accessory conical mirror 5 is chosen equal to

$$\theta = \frac{1}{2}(90^\circ + \alpha), \quad (5)$$

where α is the conical angle of the etalon object. The reflected light rays faithfully copy the traces of the illuminated light rays. The device is provided with micrometer screw 8 of the second beam-splitter 3, and with photoregistrator 9.

The light rays, reflected from the conical surface of the etalon of the industrial part 6, produce the first point-like image on the photoregistrator 9. The second point-like image is produced by the light rays reflected from the surface of the second beam-splitter 3 and then from the back surface of the first beam-splitter 2. In general case the first image can assume the form of a ring. Its diameter is a measure of the deviation of the tested conical surface from the perfect etalonic one. When this deviation is very small, and the diameter of this ring is smaller than the diffraction deblouring, these point-like spots are brought into coincidence. With micrometer screw 8 operator tunes the destructive mode of the interference picture between these two spots up to n -th diffraction wing. With this superresolution technique the sensitivity of this device can be increased n -times.

The measurement of the internal conical surfaces presents a real challenge for meso-optics. We show now a meso-optical device by means of which this difficult problem can be overcome. The problem consists in that the autocollimated mode of the illumination of the internal conical surface cannot be accomplished in the direct fashion for long conical objects. The solution of this problem is offered by the sophisticated meso-optical device [22], Fig. 22. The optical collimator 2 with central stop 3 produces ring-shaped light beam, which is converted by the circular diffraction grating 4 into the convergent conical wave. After reflection from the circular blazed reflecting grating 5, made on the conical backing, these light rays are splitted into two components. The first component as zero diffraction order of the grating 5 illuminates the tested internal conical surface 6 at small angle and will be out. The second component as plus first diffraction order of the grating 5 is reflected from the internal conical surface 6 in the autocollimated mode back to the grating 5. This time the zero diffraction order will be out as it goes parallel to the optical axis. The plus first diffraction order is propagating to the circular diffraction grating 4. The plus first diffraction order on the circular diffraction grating 4 is propagating to the lens 2 and will be out. The zero diffraction order transverse the circular diffraction grating 4 and illuminates the meso-optical element with ring response 8, which converts the conical

wavefront into the convergating sphero-conical wavefront with focal ring image in the plane of spatial frequencies. The spatial filter 9 in this plane represents a narrow opaque ring on the transparent region.

The circular blazed reflected diffraction grating 5 on the conical backing is dedicated to provide an autocollimator illuminating mode for tested conical surface. The reflected light rays are focused in the focal ring. An operator sees any azimuthal deviations of the generating line of the tested object with respect to the etalon. We present an example of this device for control of the industrial parts with conical angle of the internal cone $\alpha = 15.6^\circ$ and of length $L = 88$ mm. The axial dimension of grating 5 is equal to $L_1 = 100$ mm, and the external diameter $D = D_1 = 40$ mm. The conical angle of the conical backing of the grating 5 is equal to $\beta = 11.3^\circ$, and the grating period $d = 1.44 \mu\text{m}$. The period of the circular diffraction grating 4 is equal to $d_4 = 2.33 \mu\text{m}$. The distances are: $l_{24} = 158$ mm and $l_{48} = 168$ mm. The width of the working part of the meso-optical element with ring response $H = 47$ mm. The local period of the meso-optical element with ring response 8 is changing monotonously from $d_{max} = 5.38 \mu\text{m}$ up to $d_{min} = 1.51 \mu\text{m}$. The local period of the grating 8 on the central circle is equal to $d_0 = 2.33 \mu\text{m}$. The distance $l_{89} = 150$ mm. The effective width of the focal ring is equal to $\Delta r = \frac{\lambda}{H} l_{89} = 2 \mu\text{m}$ for $\lambda = 0.628 \mu\text{m}$. This corresponds to the measurement error $\delta\alpha \approx (0.1 - 0.2)''$ (arc sec.).

7. MESO-OPTICAL INTERFEROMETER

For precise measurements of the conical wavefronts, a multipass interference is generated in the meso-optical device [23], Fig. 23. Two semi-transparent mirrors on the conical backing 1 are mounted with distance ring 2 and with mechanical turning unit 3. The distance L between apexes of mirrors 1 is equal to $L = R/\cos(\alpha/2)$, where R is the length of the generating segment of the conical mirrors 1, and α is the conical angle of the conical backing.

When this interferometer is illuminated by the tested convergent conical wavefront through the semi-transparent conical mirror 1, a linear meso-optical crossover is generated on the axis of the interferometer. The divergent conical wavefront is falling on the semi-transparent conical mirrors and is reflected from this mirror. The process of the multipass walking of the light rays in the space between two conical mirrors is observed. If the generating line of the conical wavefront is parallel to the generating line of the semi-transparent conical mirrors 1, the pure multipass interference is taking place. The effective number of such passages is equal approximately to $(1 - \eta)^{-1}$, where η is the reflectivity of the semi-transparent conical mirrors 1.

The angular interval $\Delta\varphi_n$ between two adjacent angular directions φ_k and φ_{k-1} with maximal transmittances is defined by the equation

$$\Delta\varphi_k = \varphi_k - \varphi_{k-1} = \lambda/2L \sin \varphi_k. \quad (6)$$

The effective angular width of such a maximum of the transmittance is defined by the condition

$$\frac{2\pi L[\varphi_k^2 - (\varphi_k + \delta_\varphi)^2]}{\lambda} = \frac{1 - \eta}{2\sqrt{\eta}}, \quad (7)$$

$$\delta_\varphi = \frac{(1 - \eta)\lambda}{1\sqrt{\eta} \cdot 2\pi L \cdot \varphi_k}. \quad (8)$$

The operation of this meso-optical interferometer is performed as follows. At first, the axis of the tested conical wavefront is set in coincidence with the axis of the interferometer. Then, by means of the mechanical turning unit 4, an adjustment operation is made with the aim to get the coincidence of the angle φ with one of the angular direction φ_k with maximal transmittance. After that operation, an interference pattern produced by auxiliary lens is observed. Now we can detect azimuthal deviations in the incident conical wavefront.

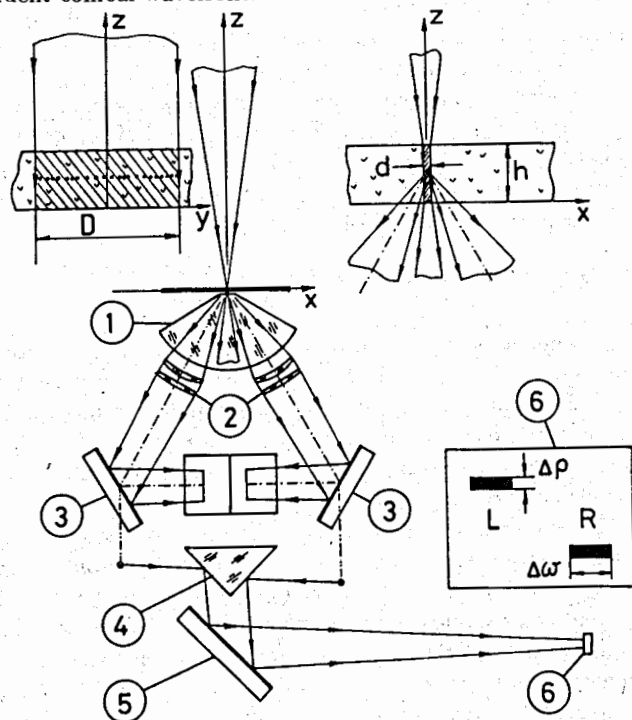


Fig. 1. Schematic diagram of the stereoscopic meso-optical Fourier transform microscope (MFTM) with double focusing: 1 — frontal spherical immersion lens, 2 — cylindrical objectives, 3 — plane mirror, 4 — double mirror, 5 — plane mirror, 6 — photosensitive matrix of the CCD-TV-camera, *L* and *R* — the left and the right meso-optical images (spots) of the straight line particle track, *d* — the width of the illuminated region, *D* — the length of the illuminated region, and *h* — the depth of the nuclear emulsion layer.

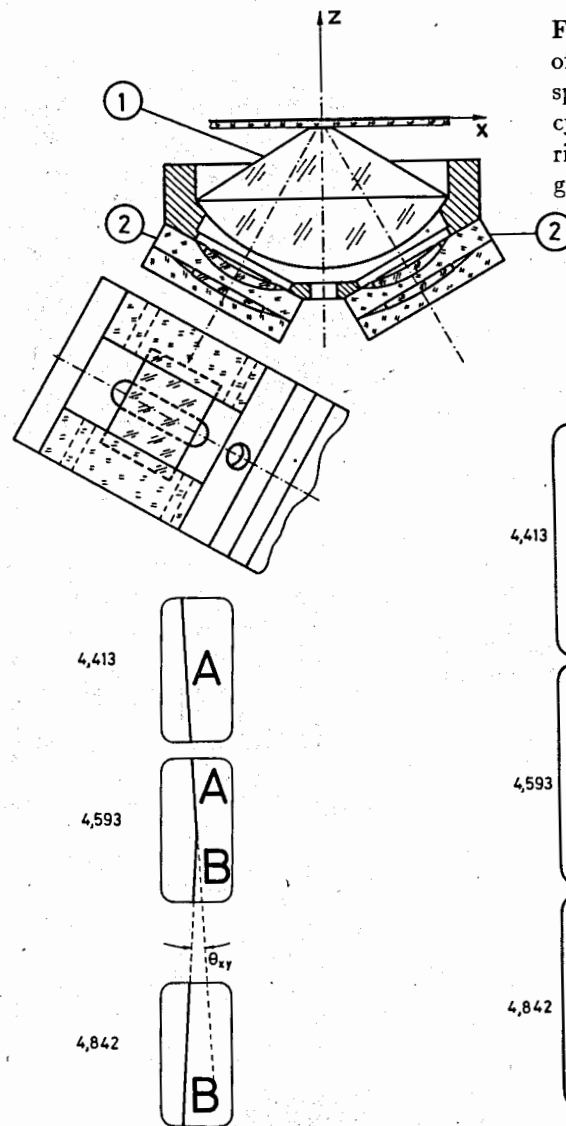


Fig. 2. The real construction of the optical block with frontal spherical lens 1 and with two cylindrical objectives 2, mounted rigidly on the elements from organic glass.

Fig. 3. Small angle scattering event $A \rightarrow B$ observed at three different longitudinal coordinates of the MFTM stage: $Y = 4.313; 4.593; 4.842$ mm.

Fig. 4. The small angle scattering event $A \rightarrow B$, presented in Fig. 3, is transformed by the MFTM into three different pictures on the photosensitive matrix of the CCD-TV-camera, presented at the same three longitudinal coordinates of the MFTM stage as in Fig. 3.

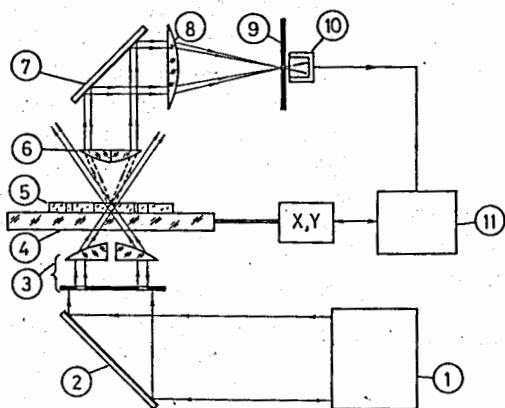


Fig. 5. Complete scheme of the new confocal microscope for selective observation of the vertical particle tracks with convergent and divergent geometries of the light rays in the illuminating and imaging objectives: 1 — laser, 2 — plane mirror, 3 — cylindrical interference illuminating system, 4 — glass support, 5 — nuclear emulsion layer with vertical particle tracks, 6 — cylindrical interference imaging system, 7 — plane mirror, 8 — lens, 9 — pinhole, 10 — photoselector, 11 — computer.

Fig. 6. Example of six vertical particle tracks marked as \odot inside the square to be scanned.

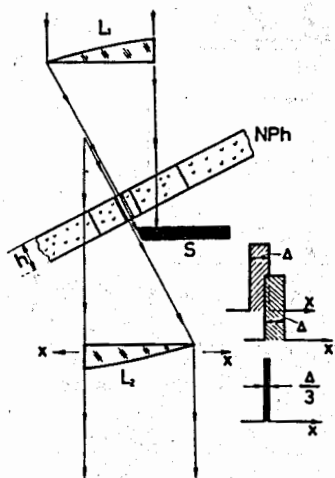
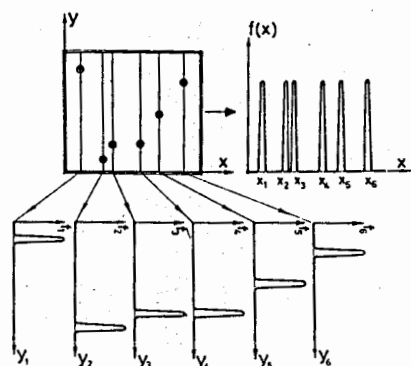


Fig. 7. Confocal caustic meso-optical microscope for selective observation of the vertical particle tracks: L_1 — illuminating cylindrical half-lens, NPh — nuclear photoemulsion layer, S — light stop, L_2 — imaging cylindrical half-lens. The moving of the half-lens L_2 is accomplished along X-axis.



Fig. 8. Caustic interference pattern produced by the illuminating cylindrical half-lens L_1 .

Fig. 9. Two coaxial conical waves of the same wavelength and interference fringes, oriented in the meridional cross section along the bisectrix of the angle between two wave vectors \vec{k}_1 and \vec{k}_2 .

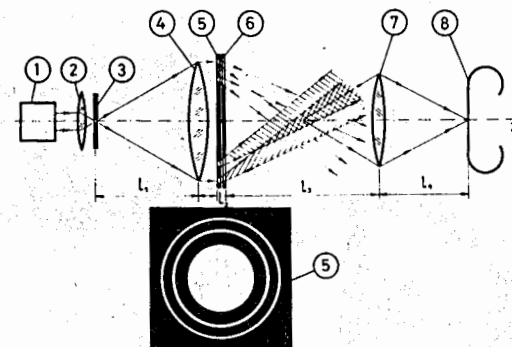
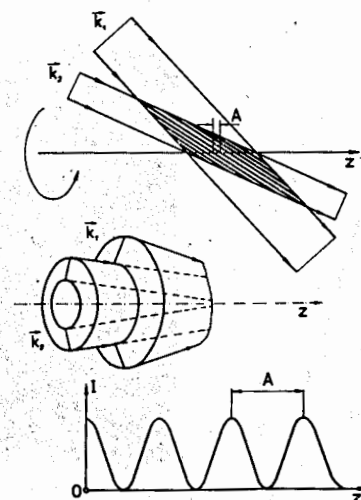


Fig. 10. The experimental arrangement for observation of the longitudinal interference of the coaxial conical wave fronts generated by narrow coaxial transmitting rings: 1 — laser, 2 — objective lens, 3 — the screen with pinhole, 4 — the second objective lens, 5 — the screen with narrow coaxial transmitting rings, 6 — the cut-off screen, 7 — the imaging objective lens, 8 — photofilm.

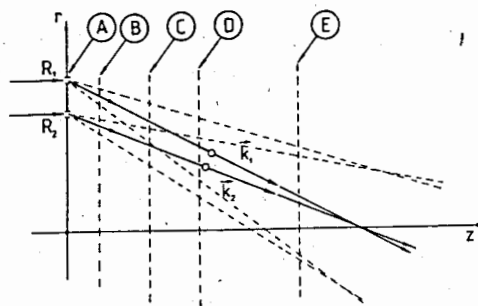


Fig. 11. Different parts of the volume between the screens 5 and 6 (generator) shown in Fig. 10, with different structures of the interference pattern: R_1 and R_2 — two narrow coaxial transmitting rings, k_1 and k_2 — wave vectors which define the corresponding quasi-conical wave fronts.

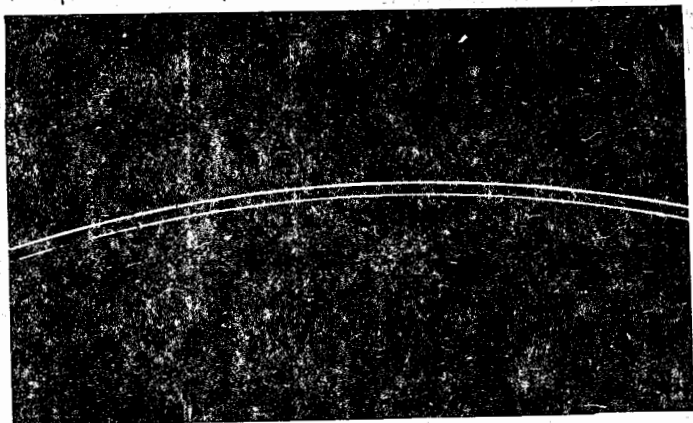


Fig. 12. The fragment of two transmitting rings in the screen 5 (Fig. 10) (plane A).

Fig. 13. The structure of the interference pattern in the plane C.

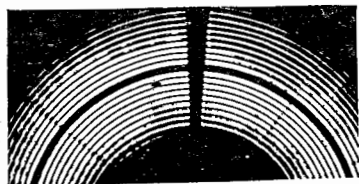
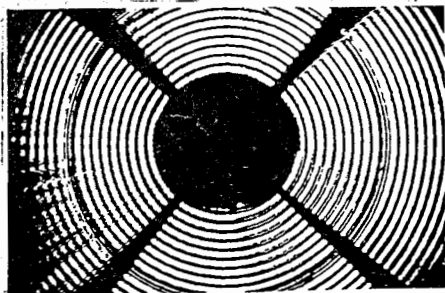


Fig. 14. The structure of the interference pattern in the region D.

Fig. 15. The structure of the interference pattern in the region E.

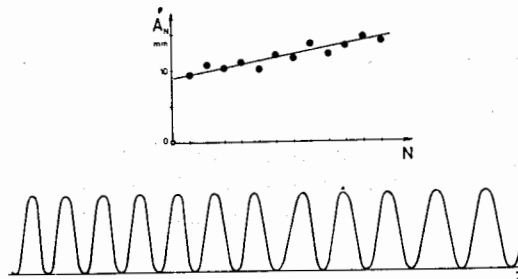
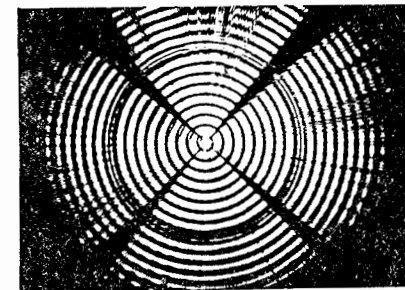


Fig. 16. Periodicity of the light intensity distribution on the optical axis and the dependence of the period A versus the ordinal number of the maximum.

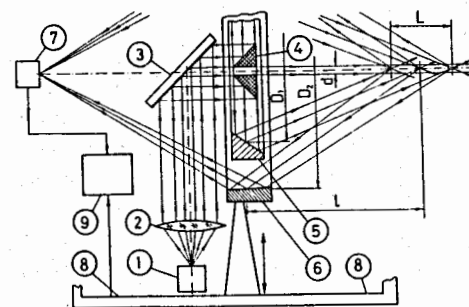


Fig. 17. Confocal meso-optical keratometer: 1 — point light source, 2 — lens, 3 — plane mirror, 4 — conical mirror with central hole, 5 — first external conical mirror, 6 — second external conical mirror, 7 — point photodetector, 8 — support, 9 — computer.

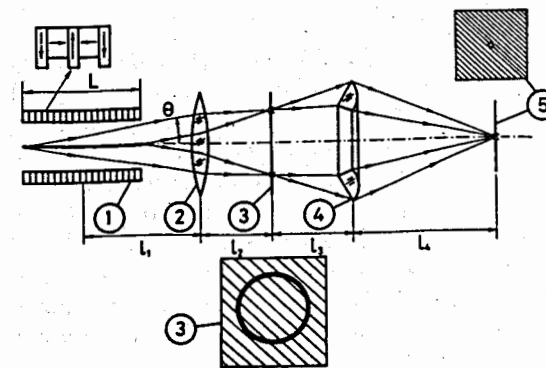


Fig. 18. Inverse meso-optical system designed to focus into the point the synchrotron radiation from undulator with $\theta \neq 0$: 1 — undulator, 2 — first inverse meso-optical objective, 3 — ring-shaped diaphragm, 4 — second inverse meso-optical objective, 5 — pin-hole diaphragm.

Fig. 19. Self-focusing undulator.

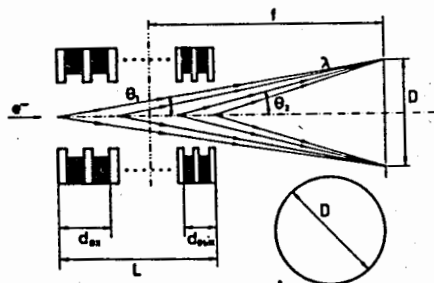
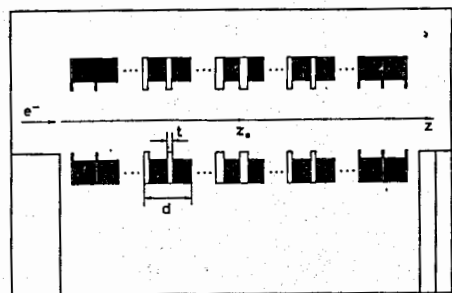


Fig. 20. Apodized undulator, where t is the thickness of the undulator magnetic element of soft magnetic material.

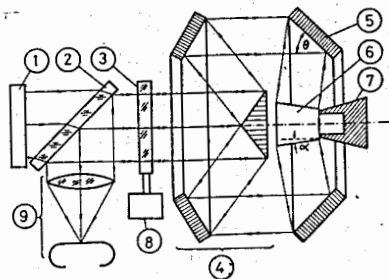


Fig. 21. Meso-optical conicometer for external conical surfaces: 1 — laser, 2 — first beam-splitter, 3 — second beam-splitter, 4 — system of two conical mirrors for producing the ring-form plane beam, 5 — accessory conical mirror, 6 — industrial part with external conical surface, 7 — support, 8 — micrometer screw, 9 — photodetector.

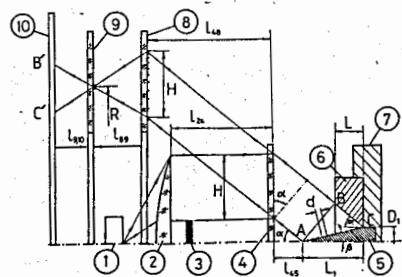
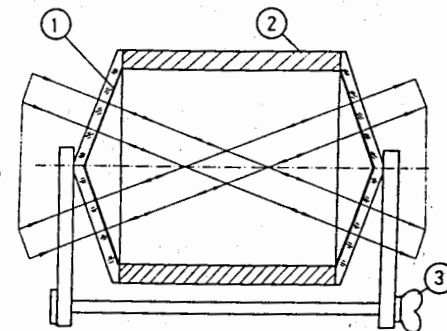


Fig. 22. Meso-optical conicometer for internal conical surfaces: 1 — point light source, 2 — lens, 3 — stop, 4 — circular diffraction grating, 5 — circular blazed reflecting grating on the conical backing, 6 — industrial part with internal conical surface to be tested, 7 — support, 8 — meso-optical element with ring response, 9 — filter of spatial frequencies, 10 — observation screen.

Fig. 23. Multipass meso-optical interferometer: 1 — semi-transparent mirror on the conical backing, 2 — distance ring, 3 — mechanical turning unit.



References

1. L.M.Soroko, *Optics, holography and mesooptics in bubble chamber of vertex detector*, Commun. JINR, D1-82-642, 1982, Dubna.
2. Gy.Bencze, L.M.Soroko, *Mesooptics and high energy physics*, Preprint JINR, E13-84-310, 1984, Dubna, Submitted to ICO-13 Congress, Sapporo, 1984.
3. A.Ya.Astakhov, Yu.A.Batusov, Gy.L.Bencze, I.Farago, A.Kisvaradi, L.Molnar, L.M.Soroko and J.Vegh, *Meso-optical Fourier Transform Microscope - a new device for high energy physics*, Nucl. Instr. Meth., **A283**, 13-23, 1989.
4. L.M.Soroko, *Meso-optical Fourier transform microscope: principles and main features*, Nucl. Tracks Radiat. Meas. **18**, 391-402, 1991.
5. L.M.Soroko, *Longitudinal interference of the diffraction free wave fields. I. Theory*, Commun. JINR, E13-90-592, 1990, Dubna.
6. L.M.Soroko, *Longitudinal interference of the diffraction free wave fields. II. Experiments*, Commun. JINR, E13-90-593, 1990, Dubna.
7. L.M.Soroko, *Longitudinal interference of the diffraction free wave fields. III. Applications*, Commun. JINR, E13-90-594, 1990, Dubna.
8. Yu.A.Batusov, L.M.Soroko, V.V.Tereshchenko, *Stereoscopic meso-optical Fourier transform microscope with double focusing*, Commun. JINR, D13-94-478, 1994, Dubna.
9. Yu.A.Batusov, V.P.Rumyantseva, L.M.Soroko, V.V.Tereshchenko, *Investigation of the geometrical distortions in the nuclear emulsion*, Commun. JINR, E13-94-502, 1994, Dubna.
10. L.M.Soroko, *Measuring technique of small scattering angles and decay length in the meso-optical Fourier transform microscope*, Commun. JINR, P13-87-170, 1987, Dubna.

11. L.M.Soroko, *A technique of the particle track curvature measurement by means of the meso-optical Fourier transform microscope*, Commun. JINR, P13-87-358, 1987, Dubna.
12. L.M.Soroko, V.V.Tereshchenko, *The technique for measuring of the dip angle of the straight particle tracks in the nuclear emulsion by means of the meso-optical Fourier transform microscope*, Commun. JINR, 13-91-204, 1991, Dubna.
13. A.Ya.Astakhov, A.Kishvaradi, V.I.Krasneslobodzev, J.Molnar, L.Molnar, L.M.Soroko, V.V.Tereshchenko, I.Torma, *Meso-optical Fourier transform microscope with one-channel photodetectors*, Commun. JINR, P13-91-299, 1991, Dubna.
14. Yu.A.Batusov, L.M.Soroko, V.V.Tereshchenko, *Fourier transform microscope of the direct observation for nuclear emulsion*, Commun. JINR, E13-91-427, 1991, Dubna.
15. L.M.Soroko, *Acceptance of the Fourier transform microscopes for nuclear emulsion*, Commun. JINR, E13-91-474, 1991, Dubna.
16. L.M.Soroko, *Meso-optical microscope of high productivity for vertical particle tracks*, Commun. JINR, E13-95-545, 1995, Dubna.
17. L.M.Soroko, *Caustical meso-optical confocal microscope for vertical particle tracks*, Commun. JINR, E13-95-546, 1995, Dubna.
18. V.P.Koronkevitch, V.P.Korolkov, A.G.Poleschuk, I.G.Palchikova, Yu.I.Yurlov, I.A.Mikhaltsova, E.G.Churin, A.P.Sokolov and A.G.Sedukhin, *Kinoforms: technologies, new elements and optical systems*, Preprint IAE SB (USSR Academy of Science) No 421 (Novosibirsk, 1989).
19. L.M.Soroko, *Inverse meso-optics and its potential applications*, Commun. JINR, E13-91-175, 1991, Dubna.
20. W.Lavander, G.Brown and T.Troxel, *Observation of X-ray undulator radiation in PEP*, Rev. Sci. Inst., 60 (1989) 1414-1418.
21. L.M.Soroko, *Measurement device*, USSR Patent No 1.730.534 (15 February 1990), Bull. No 16 (1992).
22. L.M.Soroko, *Device for measurement of the conical angle of the internal conical surfaces*, USSR Patent, No 1.737.265 (14 February 1990), Bull. No 20 (1992).
23. L.M.Soroko, *Interferometer*, USSR Patent No. 1.620.817 (17 February 1989), Bull. No 2 (1991).

Received by Publishing Department
on November 4, 1996.